

Unified theory for light-induced halide segregation in mixed halide perovskites

Zehua Chen

Eindhoven University of Technology

Geert Brocks

University of Twente

Shuxia Tao

Eindhoven University of Technology <https://orcid.org/0000-0002-3658-8497>

Peter Bobbert (✉ p.a.bobbert@tue.nl)

Eindhoven University of Technology <https://orcid.org/0000-0001-7780-7062>

Article

Keywords: halide segregations, mixed halide perovskites, thermodynamic theory

Posted Date: December 2nd, 2020

DOI: <https://doi.org/10.21203/rs.3.rs-111770/v1>

License:  This work is licensed under a Creative Commons Attribution 4.0 International License.

[Read Full License](#)

Version of Record: A version of this preprint was published at Nature Communications on May 11th, 2021. See the published version at <https://doi.org/10.1038/s41467-021-23008-z>.

1 **Unified theory for light-induced halide segregation in mixed**
2 **halide perovskites**

3 Zehua Chen^{1,2}, Geert Brocks^{1,2,4}, Shuxia Tao^{1,2}, Peter A. Bobbert^{2,3}

4 ¹*Materials Simulation and Modelling,*

5 *Department of Applied Physics, Eindhoven University of Technology,*

6 *5600 MB Eindhoven, The Netherlands*

7 ²*Center for Computational Energy Research,*

8 *Department of Applied Physics, Eindhoven University of Technology,*

9 *P.O. Box 513, 5600 MB Eindhoven, The Netherlands*

10 ³*Molecular Materials and Nanosystems,*

11 *Eindhoven University of Technology, P.O. Box 513,*

12 *NL-5600 MB Eindhoven, The Netherlands*

13 ⁴*Computational Materials Science, Faculty of Science and*

14 *Technology and MESA+ Institute for Nanotechnology,*

15 *University of Twente, P.O. Box 217,*

16 *7500 AE Enschede, The Netherlands*

17 (Dated: November 26, 2020)

18 **Abstract**

19 Mixed halide perovskites that are thermodynamically stable in the dark demix under illumination.
20 This is problematic for their application in solar cells. We present a unified thermodynamic theory
21 for this light-induced halide segregation that is based on a free energy lowering of photocarriers
22 funnelling to a nucleated phase with different halide composition and lower band gap than the par-
23 ent phase. We apply the theory to a sequence of mixed iodine-bromine perovskites. The spinodals
24 separating metastable and unstable regions in the composition-temperature phase diagrams only
25 slightly change under illumination, while light-induced binodals separating stable and metastable
26 regions appear signalling the nucleation of a low-band gap iodine-rich phase. We find that the
27 threshold photocarrier density for halide segregation is governed by the band gap difference of
28 the parent and iodine-rich phase. Partial replacement of organic cations by cesium reduces this
29 difference and therefore has a stabilizing effect.

30 Metal-halide perovskites have an extraordinary optoelectronic performance in solar en-
31 ergy harvesting and light emission applications[1–8]. The flexibility of the perovskite ABX_3
32 structure - where A is an organic or inorganic cation, B is a metal cation like Pb or Sn,
33 and X is a halide anion like I or Br - allows to stabilize a preferred phase and tune the
34 band gap through compositional alloying on different lattice sites[9–19]. Notably, mixed
35 halide perovskites have been successfully used in tandem solar cells, where the band gaps
36 in the two light-absorbing layers should be optimally tuned[18, 20, 21]. However, one of
37 the biggest problems in mixed halide perovksites is their photoinstability, specifically light-
38 induced halide segregation[17, 22–24]. Studies on mixed halide perovskites show that ex-
39 posure to continuous illumination leads to separation of the different halide ions, resulting
40 in the formation of low- and high-band gap domains. The low-band gap domains act as
41 photocarrier traps, as evidenced by redshifts in photoluminescence observations[17, 22–24].
42 The demixing is reversible, because when kept in the dark for a sufficient amount of time,
43 the perovskites return to their original mixed state. An important finding is the existence
44 of a threshold intensity for halide segregation[23, 25]. The reversibility and the existence of
45 an illumination threshold suggest a thermodynamic origin of the effect.

46 Many strategies have been proposed to suppress this halide segregation, such as enhancing
47 grain size and improving overall crystallinity[26], reducing carrier diffusion lengths[23], par-
48 tial substitution of Pb with Sn[27], application of external pressure[28], alloying Cl into the
49 I/Br lattice[29], and A-cation alloying[6, 30–32]. A-cation alloying has attracted significant
50 attention and has proven to be effective against halide segregation. It has been found that
51 MA/Cs, FA/Cs, and FA/MA/Cs mixed halide perovskites (MA stands for methylammonium
52 and FA for formamidinium) exhibit a reduced tendency for halide segregation[6, 28, 30–34].
53 In a previous study, we have shown that A-cation alloying can change the band gap by
54 changing the volume of the ABX_3 unit cell or by introducing octahedral distortions[35].
55 These structural deformations change the hybridization between the B- and X-site ions,
56 which changes the conduction band minimum and valence band maximum energies. These
57 electronic changes resulting from A-cation alloying may also contribute to phase stability
58 improvements.

59 Several explanations have been given for light-induced halide segregation. Polaron-
60 induced strain gradients under illumination have been suggested to drive the nucleation
61 of low-band gap iodine-rich domains[36, 37]. Other studies suggest that local electric fields

caused by electron-hole pairs in the thin film[38] or at the surface[39] are the driving force for ion migration and demixing. It has also been proposed that a strong gradient in carrier generation rate through the film thickness can be a driving force for halide segregation[40]. These explanations, however, do not account for the observed existence of a threshold illumination intensity for halide segregation. A model based on band gap differences between perovskites with different halide composition does account for a threshold illumination intensity[23]. In that model it is suggested that the band gap difference between mixed I/Br and I-rich domains, where photocarriers can reduce their free energy by funneling to the I-rich domains, is the driving force behind the demixing. When applied to $\text{MAPb}(\text{I}_{0.5}\text{Br}_{0.5})_3$, the model yields an illumination threshold that is of the same order of magnitude as found in a recent experiment, but it leaves the observed strong temperature dependence of the threshold unexplained[25].

There is a clear need for a unified theory for light-induced halide segregation in mixed halide perovskites that is transferable and flexible. Understanding is lacking about the influence of temperature on the illumination intensity threshold for halide segregation, but also about the role of material composition. For example, we are not aware of explanations for the improved photostability after partial Cs substitution in $\text{MAPb}(\text{I}_{1-x}\text{Br}_x)_3$ and $\text{FAPb}(\text{I}_{1-x}\text{Br}_x)_3$ [6, 28, 30–34]. From this we conclude that it is not understood how A-site alloying influences the thermodynamic stability under illumination. Such understanding is needed to avoid or mitigate the effect.

Here, we provide such a unified theory and apply it to light-induced halide segregation in $\text{MAPb}(\text{I}_{1-x}\text{Br}_x)_3$, $\text{FAPb}(\text{I}_{1-x}\text{Br}_x)_3$, $\text{CsPb}(\text{I}_{1-x}\text{Br}_x)_3$, $\text{MA}_{7/8}\text{Cs}_{1/8}\text{Pb}(\text{I}_{1-x}\text{Br}_x)_3$, and $\text{FA}_{7/8}\text{Cs}_{1/8}\text{Pb}(\text{I}_{1-x}\text{Br}_x)_3$, which are experimentally among the most studied perovskite compounds. We have added the latter two compounds to our study to investigate the influence of partial Cs substitution. The free energy for each compound in the dark is determined using binary alloying theory. By adding a contribution to the free energy from photocarriers, we obtain a parameter-free theory that enables us to construct the phase diagrams for each compound in the dark and under illumination, distinguishing stable, metastable, and unstable regions. The theory also enables us to determine the dependence of the illumination threshold for halide segregation on temperature and material composition.

92 **RESULTS**93 **Free energy in the dark.**

94 We first consider the compositional Helmholtz free energy of the five compounds, ap-
 95 plicable to the situation in the dark, within the quasi-chemical approximation (QCA, see
 96 Methods") of binary alloying theory[41]. This starts with a calculation of the configu-
 97 rational mixing enthalpy ΔU of the compounds (see Eq. (5) in "Methods"). For this we
 98 calculate within density functional theory (DFT) the energy of possible configurations of the
 99 halide anions in a supercell geometry. For the single-cation compounds $\text{MAPb}(\text{I}_{1-x}\text{Br}_x)_3$,
 100 $\text{FAPb}(\text{I}_{1-x}\text{Br}_x)_3$, and $\text{CsPb}(\text{I}_{1-x}\text{Br}_x)_3$ we take supercells with two formula units, follow-
 101 ing Brivio *et al.*[42], while for the double-cation compounds $\text{MA}_{7/8}\text{Cs}_{1/8}\text{Pb}(\text{I}_{1-x}\text{Br}_x)_3$ and
 102 $\text{FA}_{7/8}\text{Cs}_{1/8}\text{Pb}(\text{I}_{1-x}\text{Br}_x)_3$ we take supercells with eight formula units. Figs. 1a-e display for
 103 each of the five compounds the configurations with the lowest mixing enthalpy for $x = 0.5$.
 104 The mixing enthalpies per formula unit (f.u.) for the possible configurations of the I and Br
 105 anions in the supercell are given by circles in Figs. 1f-j.

106 By applying the QCA we obtain from the mixing enthalpies of the possible configurations
 107 at discrete relative Br concentrations $x = 0, 1/6, 1/3, 1/2, 2/3, 5/6, 1$ the mixing enthalpy
 108 $\Delta U(x, T)$ as a continuous function of x . The curves in Figs. 1f-j show $\Delta U(x, T)$ for dif-
 109 ferent temperatures T in the range 150-350 K. Figures 1k-o display the mixing free energy
 110 $\Delta F(x, T) = \Delta U(x, T) - T\Delta S(x, T)$ per formula unit, where $\Delta S(x, T)$ is the configurational
 111 mixing entropy.

112 In the single-cation materials, the width of the distribution in the mixing enthalpy ΔU for
 113 the different halide configurations increases in the order Cs-MA-FA of increasing cation size.
 114 The explanation is that, because of the different sizes of the halide anions (I is bigger than
 115 Br), the strain in the lattice for the different halide configurations is best accommodated
 116 for by $\text{CsPb}(\text{I}_{1-x}\text{Br}_x)_3$, followed by $\text{MAPb}(\text{I}_{1-x}\text{Br}_x)_3$ and $\text{FAPb}(\text{I}_{1-x}\text{Br}_x)_3$. The increasing
 117 cation size in this sequence is also reflected in the order of increasing unit cell volumes of
 118 the three compounds (see Supplementary Note 1). The incorporation of Cs in a relative
 119 concentration of 1/8 in $\text{MA}_{7/8}\text{Cs}_{1/8}\text{Pb}(\text{I}_{1-x}\text{Br}_x)_3$ and $\text{FA}_{7/8}\text{Cs}_{1/8}\text{Pb}(\text{I}_{1-x}\text{Br}_x)_3$ shows an ex-
 120 pected slight decrease of the width of the distribution as compared to $\text{MAPb}(\text{I}_{1-x}\text{Br}_x)_3$ and
 121 $\text{FAPb}(\text{I}_{1-x}\text{Br}_x)_3$. The width of the distribution in the mixing enthalpy affects the symmetry

¹²² $x \rightarrow 1 - x$ in the mixing free energies curves, with the curves for $\text{CsPb}(\text{I}_{1-x}\text{Br}_x)_3$ being the
¹²³ most and those for $\text{FAPb}(\text{I}_{1-x}\text{Br}_x)_3$ the least symmetric. This has an effect on the symmetry
¹²⁴ of the phase diagrams, as we will show further on.

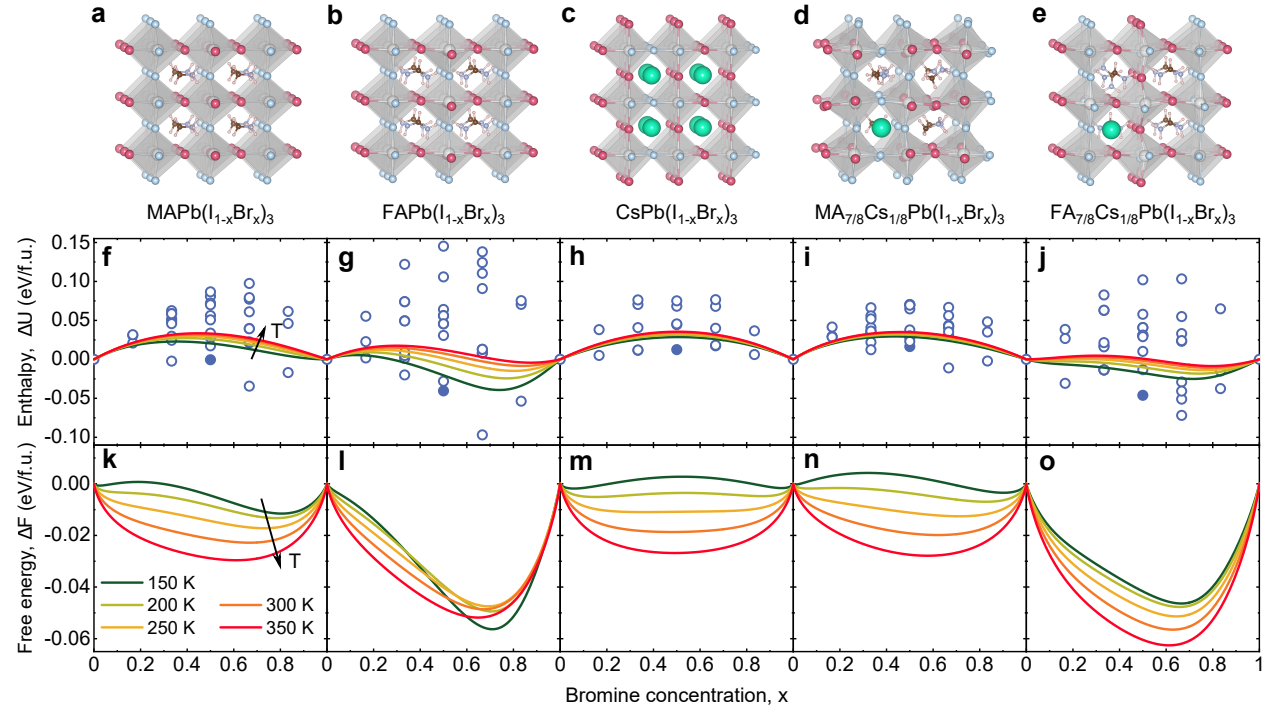
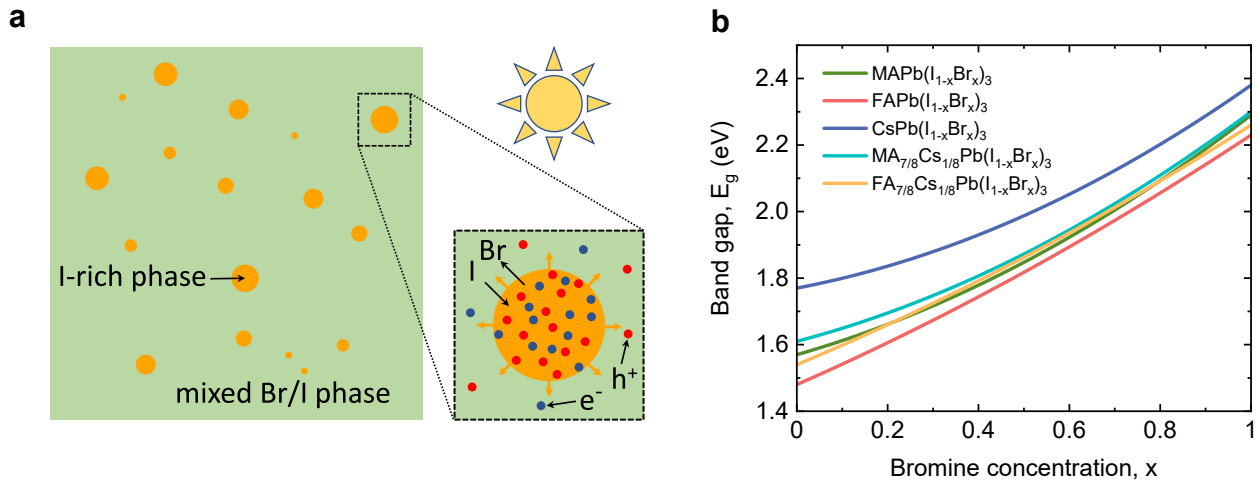


Figure 1. **Mixing enthalpy and free energy of mixed I/Br perovskites in the dark.**
(a)-(e) Atomic structures of the most stable configurations of the different compounds at relative Br concentration $x = 0.5$. Red spheres: I. Blue spheres: Br. White spheres inside octahedra: Pb. Green spheres: Cs. Cationic molecules in between octahedra: methylammonium (MA) or formamidinium (FA). **(f)-(j)** Mixing enthalpy per formula unit (f.u.) as a function of Br concentration. Circles: values calculated for each mixed configuration. Filled circles: values for the most stable configurations at $x = 0.5$, displayed in (a)-(e). Curves: results for the quasi-chemical approximation (QCA) at different temperatures. **(k)-(o)** Mixing free energy per formula unit as a function of Br concentration.

¹²⁵ **Light-induced halide segregation.**

¹²⁶ The key ingredient of our unified theory for light-induced halide segregation is the consider-
¹²⁷ ation of the combination of the compositional free energy in the dark and the free energy of

128 photocarriers in the presence of illumination. Photocarriers can reduce their free energy by
 129 funneling to low-band gap domains[23], which leads to a driving force for halide demixing,
 130 as illustrated in Fig. 2a. It is well known that halide anions in metal-halide perovskites are
 131 quite mobile. Because of stochastic fluctuations in halide composition, I-rich regions with
 132 lower band gap than the parent phase will spontaneously arise. Accumulation of diffusing
 133 photocarriers in these regions will reduce the photocarrier free energy. The free energy can
 134 then be further reduced by growth of these regions by inward diffusion of I and outward
 135 diffusion of Br, leading to nucleation of an I-rich phase and to phase separation.



136 **Figure 2. Mechanism of light-induced halide segregation. (a)** Nucleation of an I-rich phase
 137 from a mixed I/Br phase under illumination. The compositional free energy favours mixing, but
 138 this is dominated by a free energy decrease favouring demixing due to funneling of electrons and
 139 holes into low-band gap I-rich nuclei that grow by inward diffusion of I and outward diffusion of
 140 Br. **(b)** Band gap as a function of relative Br concentration x for the different compounds.

141 In our theory, band gap differences of perovskites with different halide compositions play
 142 a central role. Figure 2b shows the band gaps as a function of Br concentration x for the
 143 five compounds. The band gaps of the three single-cation perovskites are obtained from
 144 experiment[17–19], while the band gaps of the two double-cation perovskites are obtained
 145 from an interpolation scheme (see Supplementary Note 2). The differences in band gap for
 different halide compositions are mainly caused by differences in energy of the valence band
 maximum, where an increase in Br concentration decreases the energy of the valence band
 maximum[23]. So, it will be mainly the photogenerated holes that can reduce their free

¹⁴⁶ energy by funneling into I-rich domains. The electrons will follow the holes to establish local
¹⁴⁷ charge neutrality. The steepness of the band gap curves decreases for different cation com-
¹⁴⁸ positions in the order FA–FA_{7/8}Cs_{1/8}–MA–MA_{7/8}Cs_{1/8}–Cs, following the decreasing trend
¹⁴⁹ in the (average) cation size.

¹⁵⁰ Because the diffusion of photocarriers is much faster than that of the halide anions,
¹⁵¹ the distribution of the carriers over the different phases will be at any moment in time in
¹⁵² equilibrium. We define n as the density of photogenerated electrons or holes per formula unit
¹⁵³ in the mixed phase. Since $n \ll 1$, we can use Boltzmann instead of Fermi-Dirac statistics
¹⁵⁴ for the distribution of photocarriers. If phase separation occurs into two phases with Br
¹⁵⁵ concentrations x_1 and x_2 , the photocarriers will redistribute over these two phases according
¹⁵⁶ to the Boltzmann factors $\exp(-E_g(x_1)/k_B T)$ and $\exp(-E_g(x_2)/k_B T)$, where $E_g(x)$ is the
¹⁵⁷ band gap as a function of Br concentration x and $k_B T$ the thermal energy. This leads to

$$\frac{n_2}{n_1} = \exp [-(E_g(x_2) - E_g(x_1)) / k_B T], \quad (1)$$

¹⁵⁸ where n_1 and n_2 are the photocarrier densities in the two phases. With ϕ_1 and ϕ_2 the
¹⁵⁹ corresponding volume fractions of the two phases, the mixing free energy ΔF^* per formula
¹⁶⁰ unit under illumination then becomes

$$\Delta F^*(x_1, x_2, \phi_1, \phi_2, T) = \phi_1 \Delta F(x_1, T) + \phi_2 \Delta F(x_2, T) + n_1 \phi_1 E_g(x_1) + n_2 \phi_2 E_g(x_2). \quad (2)$$

¹⁶¹ Neglecting the small volume difference per formula unit between the two phases, the condi-
¹⁶² tions $\phi_1 + \phi_2 = 1$ and $\phi_1 x_1 + \phi_2 x_2 = x$ should hold. The sum of the first and second terms
¹⁶³ in Eq. (2) is the volume-weighted compositional mixing free energy in the dark. The sum of
¹⁶⁴ the third and fourth terms is the photocarrier contribution to the free energy. Because the
¹⁶⁵ band gap difference between the I-rich and parent phase is in general much larger than the
¹⁶⁶ thermal energy ($k_B T \approx 25$ meV at room temperature), even a low illumination intensity can
¹⁶⁷ according to Eq. (1) lead to a relatively large change of ΔF^* , which manifests the funneling
¹⁶⁸ effect.

¹⁶⁹ In steady state, the rate of generation of photocarriers in the system should be equal
¹⁷⁰ to the sum of the rates of photocarrier annihilation by monomolecular and bimolecular
¹⁷¹ recombination in the different phases:

$$G = \phi_1 (n_1/\tau + kn_1^2/V) + \phi_2 (n_2/\tau + kn_2^2/V). \quad (3)$$

172 Here, G is the photocarrier generation rate per formula unit, which is proportional to the
173 illumination intensity. The monomolecular and bimolecular recombination rates are given
174 by an inverse photocarrier lifetime τ and a bimolecular recombination rate constant k , for
175 which we take $\tau = 100$ ns and $k = 10^{-10}$ cm³ s⁻¹, applicable for a standard MAPbI₃
176 film[43]. For the volume per formula unit V we take the value 2.5×10^{-22} cm³ for MAPbI₃
177 (see Supplementary Note 1).

178 Equations (1)-(3) are the basis of our unified theory for light-induced halide segregation.
179 With Eqs. (1) and (3), n_1 and n_2 can be calculated for a given G . Insertion in Eq. (2) then
180 yields the mixing free energy under illumination, from which the spinodal and binodal for
181 halide phase segregation can be obtained (see “Methods”). We note that Eqs. (1)-(3) are only
182 generally applicable if the diffusion lengths of the photogenerated holes and electrons are
183 large compared to the feature sizes of the demixing. In that case an equilibrium distribution
184 of holes and electrons is established over the two phases throughout the system, with a
185 homogeneous photocarrier density in each phase. However, we will use these equations only
186 to determine the onset of phase separation. The sizes of the nuclei are then much smaller
187 than the diffusion lengths, so that the distribution of holes and electrons within the nuclei
188 is homogeneous. The distribution in the parent phase can then still be inhomogeneous, but
189 this does not affect the applicability of our theory to the onset of phase separation (see
190 Supplementary Note 3).

191 **Phase diagrams.**

192 In Figs. 3a-e we show the x - T phase diagrams for the five mixed compounds in the dark,
193 obtained from Eq. (2) for vanishing photocarrier density. The red lines are the spinodals
194 separating the metastable (grey) and unstable (pink) regions. The blue lines are the binodals
195 separating the stable (white) and metastable regions. Apart from FA_{7/8}Cs_{1/8}Pb(I_{1-x}Br_x)₃,
196 miscibility gaps appear below the critical points (x_c, T_c), where the critical temperature T_c is
197 below room temperature. This means that at room temperature the mixed compounds are
198 thermodynamically stable. The critical temperatures decrease for different cation composi-
199 tions in the order MA-FA-Cs-MA_{7/8}Cs_{1/8}. For FA_{7/8}Cs_{1/8}Pb(I_{1-x}Br_x)₃ there is no critical
200 temperature: in contrast to Figs. 1k-n no inflection points, signalling a critical point, occur
201 at low T in Fig. 1o for this compound (also for $T < 150$ K, which is the lowest T in Fig. 1o,

202 there are no inflection points). The results show that changing MA by FA as well as mixing

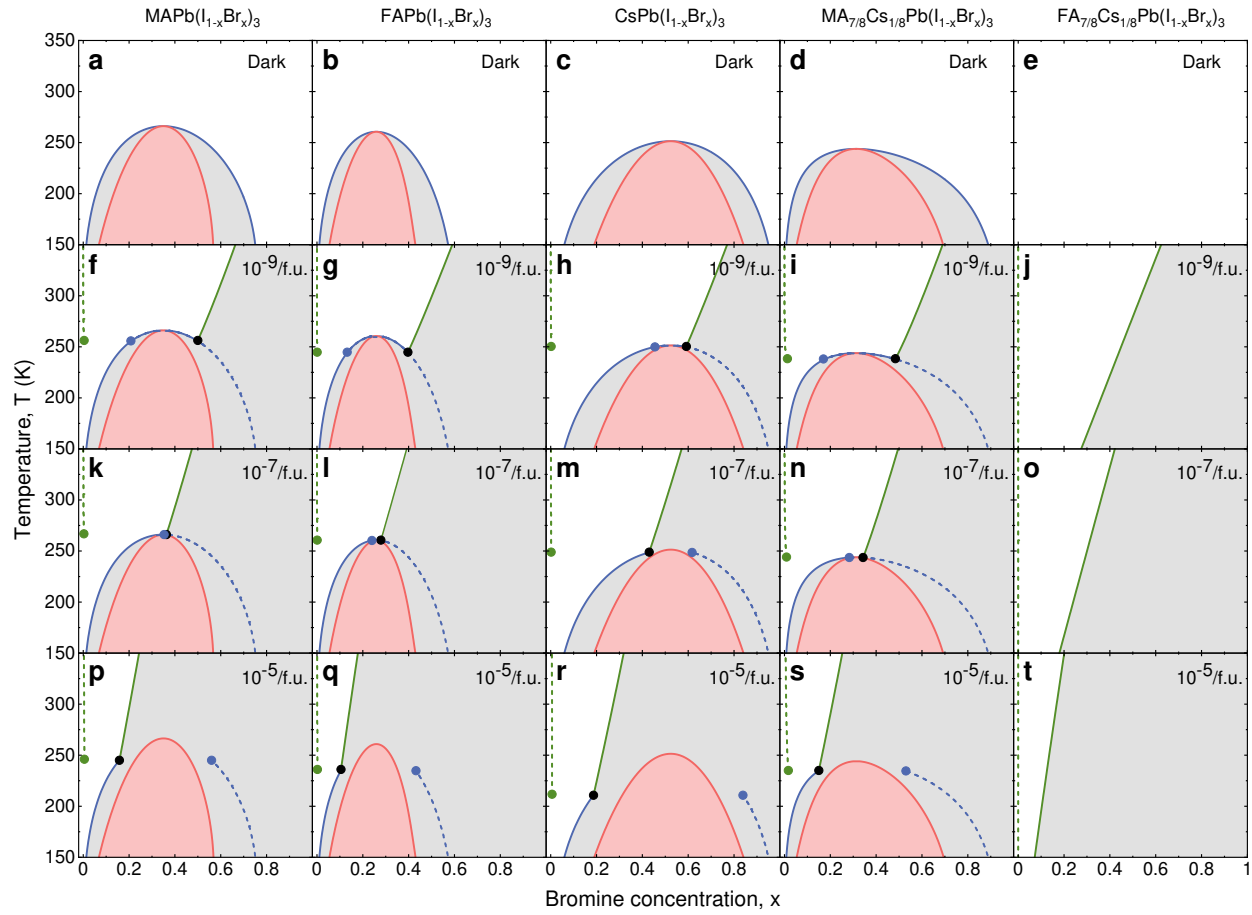


Figure 3. Phase diagrams at different photocarrier densities. (a)-(e) Phase diagrams in the dark of the different compounds in the temperature window 150-350 K. (f)-(t) Phase diagrams for photocarrier densities $n = 10^{-9}$, 10^{-7} , and 10^{-5} per formula unit. Red lines: spinodals separating the metastable (grey) and unstable (pink) regions. Full blue and green lines: binodals separating the stable (white) and metastable regions, with the blue (green) lines indicating the compositional (light-induced) binodals. When entering the metastable region by crossing the compositional (light-induced) binodals, nucleation of a phase with a Br concentration indicated by the dashed blue (green) lines becomes favourable. The dots indicate the possible coexistence of three phases: the parent phase (black dots) and two types of nucleated phases with different Br concentration (blue and green dots).

203 in Cs in the MA and FA compounds has a stabilizing effect in the dark. The amount of
204 asymmetry in the phase diagrams under the change $x \rightarrow 1 - x$ in Figs. 3a-e is in accordance

205 with the amount of asymmetry in the free energy curves shown in Figs. 1k-n.

206 We note that in the case of $\text{MAPb}(\text{I}_{1-x}\text{Br}_x)_3$ our phase diagram in the dark differs from
207 that of Brivio *et al.*[42]. In particular, our T_c of 266 K is below the value of 343 K in
208 Ref. [42]. The reason for the difference is that in Ref. [42] the symmetry lowering by the
209 specific orientation of the MA cations is neglected, leading to a reduction of the number of
210 considered different configurations of the halide anions. The finding that our T_c is below
211 room temperature is in agreement with the observation that $\text{MAPb}(\text{I}_{1-x}\text{Br}_x)_3$ does not phase
212 separate at room temperature in the dark[22].

213 Figures 3f-t show the phase diagrams of the five compounds under illumination, obtained
214 from Eqs. (1)-(3) for different photocarrier densities in the mixed state of $n = 10^{-9}$, 10^{-7} ,
215 and $10^{-5}/\text{f.u.}$ Using an absorption coefficient $\alpha = 10^5 \text{ cm}^{-1}$ and a photon energy $h\nu = 3$
216 eV[23], a value of $n = 5 \times 10^{-7}$ corresponds to an illumination intensity $I = 100 \text{ mW}$
217 cm^{-2} of approximately 1 sun ($n \approx I\alpha V\tau/h\nu$ when we neglect bimolecular recombination
218 in the mixed state). We observe that the spinodals only slightly change with increasing
219 photocarrier density. By contrast, important changes occur in the behaviour of the binodals
220 with increasing n . Our theory predicts the existence of *two* types of binodals. The first type
221 (full blue lines) can be viewed as a modification of the dark binodals by the illumination,
222 which we will call “compositional binodals”. Under illumination, a new type of binodals
223 appears (full green lines), which we will call “light-induced binodals”.

224 With increasing photocarrier density, the phase diagrams fall into two categories, ob-
225 servable for all compounds except $\text{FA}_{7/8}\text{Cs}_{1/8}\text{Pb}(\text{I}_{1-x}\text{Br}_x)_3$. (1) At low photocarrier density
226 $n = 10^{-9}/\text{f.u.}$ (Figs. 3f-i) the compositional binodals connect to the light-induced binodals
227 *after* the critical point and both left and right branches of the binodals exist. When the
228 left (right) branches of the compositional binodals are crossed by increasing (decreasing)
229 x or decreasing T , a phase is nucleated that is Br-richer (I-richer) than the parent phase,
230 indicated by the dashed blue lines. We note that the dashed blue lines do not exactly co-
231 incide with the full blue lines at the top of the binodals. (2) At high photocarrier density
232 $n = 10^{-5}/\text{f.u.}$ (Figs. 3p-s) the compositional binodals connect to the green binodals *before*
233 the critical point and only left branches of the compositional binodals exist. Figure 3k dis-
234 plays for $\text{MAPb}(\text{I}_{1-x}\text{Br}_x)_3$ a phase diagram that is very close to the transition between the
235 two categories of phase diagrams, whereas Figs. 3l-n show both category-1 and category-2
236 phase diagrams for $\text{FAPb}(\text{I}_{1-x}\text{Br}_x)_3$, $\text{CsPb}(\text{I}_{1-x}\text{Br}_x)_3$, and $\text{MA}_{7/8}\text{Cs}_{1/8}\text{Pb}(\text{I}_{1-x}\text{Br}_x)_3$.

237 For both categories of phase diagrams, a phase is nucleated that is I-richer than the
 238 parent phase when the light-induced binodals are crossed by increasing x or decreasing T ,
 239 as indicated by the green dashed lines. Interestingly, triple points $(x_{\text{tr}}, T_{\text{tr}})$ exist where two
 240 different phases with different halide composition can be nucleated from the parent phase.
 241 The Br concentrations of the parent phase (x_{tr}) and the two phases that can be nucleated
 242 at the triple points are indicated by dots in Fig. 3. For category-1 phase diagrams the Br
 243 concentrations of the nucleated phases at the triple points (blue and green dots) both have
 244 a lower Br concentration than the parent phase (black dot), whereas for category-2 phase
 245 diagram one nucleated phase is Br-richer and the other is I-richer than the parent phase. The
 246 predictions of two categories of phase diagrams and the existence of triple points are unique
 247 features of our theory. Their experimental observation by careful experimentation would be
 248 extremely interesting and could substantially increase our knowledge of light-induced halide
 249 segregation.

250 **Threshold photocarrier densities.**

251 Figure 4 shows for the five compounds results for the threshold photocarrier density n_t
 252 for halide segregation. This is the value of n at which the light-induced binodals are crossed
 253 for a given Br concentration x and temperature T (the full green lines in Figs. 3f-t). The
 254 light-induced nucleated phase is almost 100% I-rich (see the dashed green lines in Figs. 3f-t).
 255 From this fact, the following very accurate expression can be derived for n_t (see “Methods”):

256

$$n_t \approx f(x, T) \exp(-\Delta E_g(x)/k_B T), \quad (4)$$

257 where $\Delta E_g(x) \equiv E_g(x) - E_g(0)$. The prefactor in this expression is
 258 $f(x, T) \equiv \sqrt{(-\Delta F(x, T) + x \partial_x \Delta F(x, T)) V / k \tau E_g(x)}$. Equation (4) predicts extremely
 259 low thresholds n_t at room temperature. We note that n_t is the threshold photocarrier
 260 density in the mixed phase or in the parent phase at the onset of phase separation. The
 261 photocarrier density in the nucleated phase is according to Eq. (1) much larger. For exam-
 262 ple, for MAPb(I_{0.5}Br_{0.5})₃ we have $\Delta E_g(x = 0.5) \approx 0.28$ eV (see the green line in Fig. 2b), so
 263 that the photocarrier density in the almost I-pure nucleated phase is at room temperature a
 264 factor of about 7×10^4 larger. This also means that, while the bimolecular recombination in
 265 the mixed or in the parent phase is negligible, this is definitely not the case in the nucleated

266 phase.

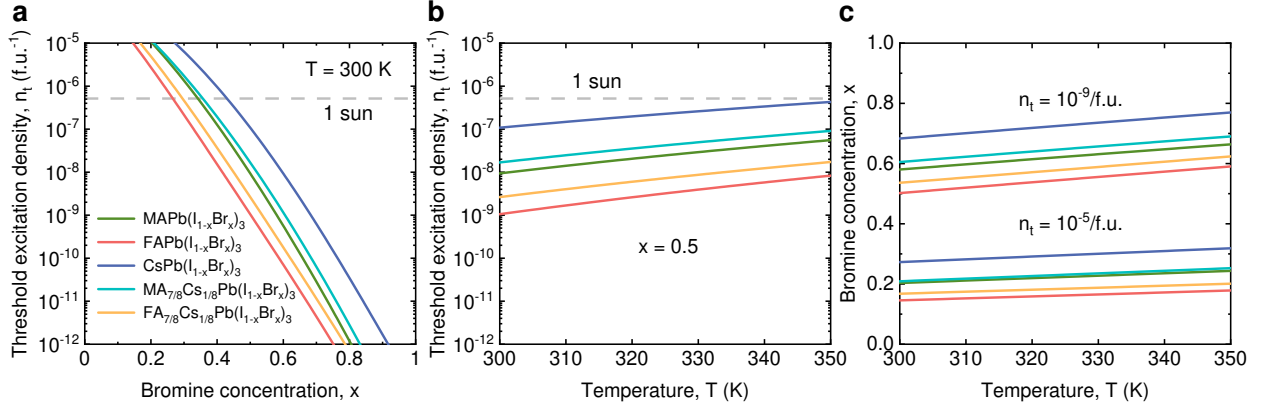


Figure 4. **Threshold photocarrier density for light-induced halide segregation.** (a) Threshold photocarrier density n_t for the different compounds at room temperature $T = 300$ K for light-induced halide segregation, as a function of Br concentration x . (b) Threshold photocarrier density as a function of temperature for $x = 0.5$. The horizontal dashed line in (a) and (b) indicates the photocarrier density $n = 5 \times 10^{-7}$ /f.u. in the mixed phase for about 1 sun illumination. (c) Bromine concentration as a function of temperature at threshold photocarrier densities $n_t = 10^{-9}$ and 10^{-5} /f.u.

267 In Fig. 4a we show n_t as a function of Br concentration x at room temperature. Apart
 268 from the extremely low n_t , an extremely strong dependence on x is found. The threshold
 269 n_t increases for different cation composition in the order FA–FA_{7/8}Cs_{1/8}–MA–MA_{7/8}Cs_{1/8}–
 270 Cs, which is the same order as the decrease in the steepness of the band gap curves in
 271 Fig. 2b. This order and the extremely strong dependence of n_t on x can be explained
 272 from the exponential factor $\exp(-\Delta E_g(x)/k_B T)$ in Eq. (4). We thus come to the important
 273 conclusion that the threshold photocarrier density is governed by the band gap difference of
 274 the mixed halide compound and the I-pure compound.

275 In Fig. 4b we show the T -dependence of n_t at Br concentration $x = 0.5$ and in Fig. 4c
 276 the T -dependence of x at a low, $n_t = 10^{-7}$ /f.u., and a high, $n_t = 10^{-3}$ /f.u., threshold
 277 photocarrier density. Both figures cover the temperature interval 300–350 K, which is a
 278 relevant operational range for solar cells. All curves in Fig. 4b are below the photocarrier
 279 density $n = 5 \times 10^{-7}$ /f.u. at 1 sun (dashed horizontal line), showing that all compounds
 280 with equal amounts of Br and I segregate at 1 sun illumination. The steepness of the

281 curves in Fig. 4b follows the same order as the steepness of the band gap curves in Fig. 2b.
282 For both values of n_t the curves in Fig. 4c show a decrease in steepness for the different
283 compounds with an order that is opposite to the order in which the steepness of the band
284 gap curves decreases. At the same time, the steepness of the curves for all compounds
285 increases approximately proportionally to the logarithm of n_t . All these observations can be
286 explained from the exponential factor $\exp(-\Delta E_g(x)/k_B T)$ in Eq. (4), although the factor
287 $f(x, T)$ also contributes somewhat to the T -dependence.

288 Our results for the photostability of the different compounds agree with experimen-
289 tally observed trends. Firstly, we find that $\text{CsPb}(\text{I}_{1-x}\text{Br}_x)_3$ is more photostable than
290 $\text{MAPb}(\text{I}_{1-x}\text{Br}_x)_3$. This is consistent with the experimental observations that $\text{MAPb}(\text{I}_{1-x}\text{Br}_x)_3$
291 is found to segregate for bromine concentrations $0.2 < x < 1$ [22, 40], while $\text{CsPb}(\text{I}_{1-x}\text{Br}_x)_3$
292 shows a smaller instability range $0.4 < x < 1$ [17]. Secondly, we find that partial Cs alloying
293 improves photostability, which is an agreement with the observed enhanced photostability
294 by partial substitution of the organic cation in $\text{MAPb}(\text{I}_{1-x}\text{Br}_x)_3$ and $\text{FAPb}(\text{I}_{1-x}\text{Br}_x)_3$ by
295 Cs[6, 28, 30–34].

296 Using $\text{MAPb}(\text{I}_{0.5}\text{Br}_{0.5})_3$ as an example, we predict at 300 K a photocarrier density thresh-
297 old of $n_t = 9 \times 10^{-9}/\text{f.u.}$ (see the green line in Fig. 4b), corresponding to an illumina-
298 tion threshold of $1750 \mu\text{W cm}^{-2}$. In the recent experiments of Ref. [25] a threshold for
299 $\text{MAPb}(\text{I}_{0.5}\text{Br}_{0.5})_3$ of about $35 \mu\text{W cm}^{-2}$ is reported. We also predict an increase of the illu-
300 mination threshold by a factor 5.5 between 300 and 350 K, as compared to the experimentally
301 found increase by a factor of about 3[25]. Considering the extremely strong sensitivity of
302 n_t to the various quantities in our theory, we find the agreement satisfactory. We note in
303 particular the extremely strong dependency of n_t on the Br concentration x (see Fig. 4a),
304 which leads to an extremely large sensitivity of the illumination threshold to preparation
305 details of the perovskite film.

306 We remark that our theory has no adjustable parameters and can be the starting point
307 for the inclusion of effects that were not yet accounted for. One such effect could be that
308 the number of defects in the nucleated phase is larger than in the parent phase, possibly
309 caused by a lattice mismatch between the two phases. This could lead to a lower photocarrier
310 lifetime τ in the nucleated phase, which presently is assumed to be the same as in the parent
311 phase. A lower τ in the nucleated phase will lead to a lower n_t . Another effect that will lower
312 n_t is a lattice compression of the I-rich nuclei by the surrounding mixed parent phase with

313 smaller lattice constant, leading to a lowering of the band gap in the nucleated phase. If we
314 take for MAPbI_3 under compressional strain the $\text{MAPb}(\text{I}_{0.5}\text{Br}_{0.5})_3$ lattice constant instead
315 of its relaxed lattice constant, we find that the calculated DFT band gap is decreased by
316 0.145 eV. Using Eq. (4), this implies a decrease in n_t by a factor of about 300 at room
317 temperature and thus a 6 times lower illumination threshold than in the experiment of
318 Ref. [25]. In reality, the lattice adjustment to the surrounding phase will not be complete,
319 so that a refined analysis may lead to a result in closer agreement with the experiment.

320 **DISCUSSION**

321 We have presented a unified thermodynamic theory for light-induced halide segrega-
322 tion in mixed halide perovskites. The theory is based on minimization of the sum of a
323 compositional free energy, obtained from binary alloying theory, and an electronic free
324 energy of photocarriers, which distribute thermally over a nucleated phase and a parent
325 phase with different band gaps due to different I-Br compositions. We applied the the-
326 ory to $\text{MAPb}(\text{I}_{1-x}\text{Br}_x)_3$, $\text{FAPb}(\text{I}_{1-x}\text{Br}_x)_3$, $\text{CsPb}(\text{I}_{1-x}\text{Br}_x)_3$, as well as the partial Cs com-
327 pounds $\text{MA}_{7/8}\text{Cs}_{1/8}\text{Pb}(\text{I}_{1-x}\text{Br}_x)_3$ and $\text{FA}_{7/8}\text{Cs}_{1/8}\text{Pb}(\text{I}_{1-x}\text{Br}_x)_3$. The spinodals in the Br
328 concentration-temperature, $x-T$, phase space, separating unstable and metastable regions,
329 only slightly change for photocarrier densities corresponding to relevant illumination in-
330 tensities. In addition to compositional binodals that are also present in the dark, new
331 light-induced binodals appear, signalling the nucleation of an I-rich phase from the parent
332 phase. These binodals, which are attributed to funneling of photocarriers into the low-band
333 gap I-rich phase, occur at an extremely small photocarrier density and illumination inten-
334 sity governed by the band gap difference between the mixed phase and the nucleated I-rich
335 phase.

336 Several predictions of the theory are in agreement with experimental finding, such as a
337 strongly temperature and composition dependent illumination threshold for halide segregag-
338 tion and a stabilization effect upon alloying FA or MA with Cs. The fundamental reason of
339 this stabilization effect is that mixing Cs into FA or MA reduces the unit cell volume, leading
340 to smaller band gap differences between the parent and I rich phases. The theory predicts
341 two categories of phase diagrams and the existence of photocarrier density-dependent triple
342 points $(x_{\text{tr}}, T_{\text{tr}})$ below room temperature, where two phases with different Br-I compositions

343 can be nucleated from the parent phase. The experimental study of these novel physical
344 phenomena would be extremely interesting and increase our understanding of light-induced
345 halide segregation. The theory is flexible and transferable, making it a suitable starting
346 point for refinements to include effects that have not yet been considered, such as different
347 recombination rates in the different phases and changes in the band gap due to strain. The
348 theory can also be readily applied to other semiconductors where the band gap is tuned by
349 alloying.

350 We finally note that a metastable region in phase space is entered when the illumination
351 intensity exceeds the threshold for halide segregation. According to nucleation theory, a
352 surface free energy due to the presence of an interface between the nucleated and parent
353 phase could inhibit phase separation. Phase separation then requires the crossing of a free
354 energy barrier composed of a positive surface free energy and the negative bulk free energy
355 for a nucleus of a critical size. For the investigation of a phase separation inhibition effect
356 it would be important to evaluate the surface free energy between a mixed I-Br and an
357 I-rich phase, and the probability that a nucleus will grow spontaneously to a critical size.
358 Differences in surface free energy and sizes of critical nuclei for different perovskites could
359 provide additional handles to suppress light-induced halide segregation.

360 **METHODS**

361 **Calculation of total energies**

362 To calculate the total energies of the single-cation mixed halide perovskites
363 $\text{MAPb}(\text{I}_{1-x}\text{Br}_x)_3$, $\text{FAPb}(\text{I}_{1-x}\text{Br}_x)_3$, and $\text{CsPb}(\text{I}_{1-x}\text{Br}_x)_3$, we start from a periodic super-
364 cell of the pure I compounds containing 2 formula units, with a $2 \times 1 \times 1$ expansion of a
365 (pseudo)cubic perovskite building block. We then replace I anions by Br anions at different
366 concentrations $x = 0, 1/6, 1/3, 1/2, 2/3, 5/6, 1$. The total number of possible configurations
367 for each single-cation perovskite is $2^6 = 64$. For the Cs perovskite with perfect O_h symmetry
368 the three halide sites are equivalent, which reduces the total number of inequivalent configu-
369 rations to 21. Accounting for the deviation from O_h symmetry in the case of the MA and FA
370 perovskites leads to an increase to 36 inequivalent configurations. To include the Cs cations
371 in the double-cation perovskites $\text{MA}_{7/8}\text{Cs}_{1/8}\text{Pb}(\text{I}_{1-x}\text{Br}_x)_3$ and $\text{FA}_{7/8}\text{Cs}_{1/8}\text{Pb}(\text{I}_{1-x}\text{Br}_x)_3$, the
372 $2 \times 1 \times 1$ supercells of the 36 inequivalent $\text{MAPb}(\text{I}_{1-x}\text{Br}_x)_3$ and $\text{FAPb}(\text{I}_{1-x}\text{Br}_x)_3$ configura-
373 tions are repeated in two directions to construct $2 \times 2 \times 2$ supercells containing 8 formula
374 units. The double-cation perovskites are then constructed by substituting one of the 8
375 organic cations by Cs. The total number of inequivalent configurations is then $2 \times 36 = 72$,
376 where the factor 2 reflects the two inequivalent Cs substitutions in the $2 \times 2 \times 2$ supercell.

377 The total energy calculations are performed within Density-Functional Theory (DFT).
378 We use the projected augmented wave (PAW) [44] method and the Perdew-Burke-Ernzerhof
379 exchange-correlation functional revised for solids (PBEsol) [45] within the generalized gra-
380 dient approximation (GGA)[46], as implemented in the Vienna *ab initio* simulation package
381 (VASP)[47]. We use $4 \times 8 \times 8$ and $4 \times 4 \times 4$ k -point Brillouin zone samplings for the single-
382 cation and double-cation compounds, respectively, and a plane-wave kinetic energy cutoff
383 of 500 eV. The shape and volume of the unit cell as well as the atomic positions in the unit
384 cell of each configuration are fully optimized. The energy and force convergence parameters
385 are set at 0.01 meV and 0.005 eV/ \AA , respectively.

386 **Calculation of the mixing free energy**

387 The mixing enthalpies ΔU_j per formula unit of the inequivalent configurations $j = 1, \dots J$
 388 with relative Br concentration x are given by

$$\Delta U_j = E_j - (1 - x)E_{\text{APbI}_3} - xE_{\text{APbBr}_3}, \quad (5)$$

389 where E_j , E_{APbI_3} , and E_{APbBr_3} are the total energies per formula unit of configuration j ,
 390 the pure I configuration, and the pure Br configuration, respectively. “A” denotes MA, FA,
 391 Cs, $\text{MA}_{7/8}\text{Cs}_{1/8}$, or $\text{FA}_{7/8}\text{Cs}_{1/8}$. The resulting enthalpies are given by the $J = 36$ points
 392 in Figs. 1f and g for $\text{MAPb}(\text{I}_{1-x}\text{Br}_x)_3$ and $\text{FAPb}(\text{I}_{1-x}\text{Br}_x)_3$, respectively, and the $J = 21$
 393 points in Fig. 1h for $\text{CsPb}(\text{I}_{1-x}\text{Br}_x)_3$. To treat the double-cation perovskites on the same
 394 footing as the single-cation perovskites we take the average of the total energies of the two
 395 inequivalent Cs substitutions, resulting in enthalpies given by the $J = 36$ points in Figs. 1i
 396 and j. We checked that the mixing free energy curves (see below) for the two inequivalent
 397 Cs substitutions are almost indistinguishable, which validates taking this average.

398 We apply the quasi-chemical approximation (QCA)[41] to obtain the mixing enthalpy
 399 $\Delta U(x, T)$, entropy $\Delta S(x, T)$, and Helmholtz free energy $\Delta F(x, T)$ as functions of the Br
 400 concentration x and temperature T . The QCA has been successfully employed in the ther-
 401 modynamic analysis of semiconductor alloys[42, 48, 49]. In the QCA, the perovskite lattice
 402 is decomposed into microclusters, which are treated independently[41]. For the different
 403 microclusters we take the J inequivalent configurations mentioned above. In the QCA, the
 404 thermal equilibrium fraction of microclusters with configuration j is given by

$$\bar{x}_j = \frac{g_j \exp \{ [n_j(\text{Br})\mu_{\text{Br}} - \Delta U_j] / k_B T \}}{\sum_j g_j \exp \{ [n_j(\text{Br})\mu_{\text{Br}} - \Delta U_j] / k_B T \}}, \quad (6)$$

405 where g_j is the degeneracy and $n_j(\text{Br}) = 0, 1, 2, 3$ the number of Br anions per formula unit
 406 of the configuration, and μ_{Br} is the Br chemical potential. This chemical potential should
 407 be determined such that the desired Br concentration is obtained:

$$\sum_j n_j(\text{Br}) \bar{x}_j = 3x. \quad (7)$$

408 After having found μ_{Br} from this condition, the mixing enthalpy and entropy per formula
 409 unit are obtained as:

$$\Delta U(x, T) = \sum_j \bar{x}_j \Delta U_j, \quad (8)$$

⁴¹⁰ and

$$\Delta S(x, T) = -3k_B \left[(1-x) \ln(1-x) + x \ln x + \sum_j \bar{x}_j \ln(\bar{x}_j/x_j^0) \right], \quad (9)$$

⁴¹¹ with $x_j^0 = g_j x^{n_j(\text{Br})} (1-x)^{3-n_j(\text{Br})}$. The mixing free energy is finally obtained as $\Delta F(x, T) =$
⁴¹² $\Delta U(x, T) - T\Delta S(x, T)$.

⁴¹³ Determination of the binodals and spinodals

⁴¹⁴ To find the binodals we consider the possibility, starting from the mixed situation with
⁴¹⁵ Br concentration x , to decrease the free energy by demixing through nucleation of a phase
⁴¹⁶ with a concentration $x_2 \neq x$ with a small volume fraction $\delta\phi \equiv \phi_2$. In the mixed situation
⁴¹⁷ we can make the simplifying approximation $n \approx G/\tau$ for the photocarrier density, because
⁴¹⁸ for all relevant illumination intensities bimolecular recombination is then negligible. The
⁴¹⁹ free energy Eq. (2) in the mixed situation is $\Delta F^*(x, x, 1, 0, T)$, while the free energy in the
⁴²⁰ demixed situation is $\Delta F^*(x_1, x_2, 1 - \delta\phi, \delta\phi, T)$, with, to linear order in $\delta\phi$,

$$x_1 = x - (x_2 - x)\delta\phi. \quad (10)$$

⁴²¹ The difference in free energy between the demixed and mixed situations is then to linear
⁴²² order in $\delta\phi$:

$$\begin{aligned} \delta\Delta F^* &= \delta\phi \left\{ \Delta F(x_2, T) - \Delta F(x, T) - (x_2 - x)\partial_x \Delta F(x, T) \right. \\ &\quad + n \left[\exp\left(-\frac{E_g(x_2) - E_g(x)}{k_B T}\right) (E_g(x_2) - E_g(x)) - (x_2 - x)E'_g(x) \right] \\ &\quad \left. - n^2 k \tau \exp\left(-2\frac{E_g(x_2) - E_g(x)}{k_B T}\right) E_g(x)/V \right\}, \end{aligned} \quad (11)$$

⁴²³ with $\partial_x \Delta F(x, T) \equiv \partial \Delta F(x, T) / \partial x$. When $\delta\Delta F^* < 0$, the demixed situation has a lower
⁴²⁴ free energy than the mixed situation. We thus find the binodals in Fig. 3 for a certain
⁴²⁵ photocarrier density n by looking in x - T phase space for a value of x_2 of a nucleated phase
⁴²⁶ for which $\delta\Delta F^* = 0$. The dashed lines in Fig. 3 give the Br concentration x_2 of the nucleated
⁴²⁷ phase. For the light-induced binodals x_2 is very small, indicating the nucleation of a low-
⁴²⁸ band gap I-rich phase. When we put $x_2 = 0$ in Eq. (11) we get

$$\begin{aligned} \delta\Delta F^* &\approx \delta\phi \left\{ -\Delta F(x, T) + x\partial_x \Delta F(x, T) + n \left[-\Delta E_g(x) \exp\left(\frac{\Delta E_g(x)}{k_B T}\right) + xE'_g(x) \right] \right. \\ &\quad \left. - n^2 k \tau \exp\left(2\frac{\Delta E_g(x)}{k_B T}\right) E_g(x)/V \right\}, \end{aligned} \quad (12)$$

429 where $\Delta E_g(x) = E_g(x) - E_g(0)$ is the band gap difference between the mixed and the
 430 pure I phase. The term $xE'_g(x)$ is found to be very small and can be neglected. Putting
 431 $\delta\Delta F^* = 0$ and solving for n yields the threshold photocarrier density Eq. (4), which provides
 432 an extremely good approximation to the curves in Fig. 4.

433 To find the spinodals we consider the possibility to decrease the free energy by generating
 434 a volume fraction ϕ of a phase with a slightly different concentration $x_2 = x + \delta x$. The free
 435 energies in the demixed situation can now be written as $\Delta F^*(x - \phi\delta x/(1 - \phi), x + \delta x, 1 -$
 436 $\phi, \phi, T)$. To second order in δx the difference in free energy then becomes

$$\delta\Delta F^* = \frac{\phi(\delta x)^2}{2(1 - \phi)} \left\{ \partial_x^2 \Delta F(x, T) + n \left[-2 \frac{(E'_g(x))^2}{k_B T} + E''_g(x) \right] \right\}. \quad (13)$$

437 When $\delta\Delta F^* < 0$, the demixed situation can be established from the mixed situation in a
 438 continuous way, without crossing a free energy barrier. Putting $\delta\Delta F^* = 0$ thus yields the
 439 spinodal separating the metastable from the unstable region in x - T phase space.

440 We note that for the unilluminated case ($n = 0$, see the top panels in Fig. 3) the above
 441 procedures to find the binodals and spinodals are identical to the usual procedures, where
 442 the binodals are found from a common tangent construction and the spinodals from the
 443 inflection points of ΔF as a function of x . These usual procedures can be applied when the
 444 mixing free energy is equal to the volume-weighted sum of the free energies per volume of
 445 the different phases, which holds in the dark but not under illumination.

446 Data availability

447 Data supporting this publication are available from the corresponding author on request.
 448 The calculated volumes of the unit cells of the perovskites studied in this work are given in
 449 Supplementary Fig. S1. The used formulas for the band gaps of the perovksites are given in
 450 Supplementary Table SI.

451 Code availability

452 The DFT calculations were performed with the code VASP (“Vienna Ab initio Simulation
 453 Package”), available at www.vasp.at.

-
- 454 [1] Kojima, A., Teshima, K., Shirai, Y. & Miyasaka, T. Organometal halide perovskites as
455 visible-light sensitizers for photovoltaic cells. *J. Am. Chem. Soc.* **131**, 6050–6051 (2009).
- 456 [2] Green, M. A., Ho-Baillie, A. & Snaith, H. J. The emergence of perovskite solar cells. *Nat.*
457 *Photonics* **8**, 506–514 (2014).
- 458 [3] Noel, N. K. *et al.* Lead-free organic-inorganic tin halide perovskites for photovoltaic applica-
459 tions. *Energy Environ. Sci.* **7**, 3061–3068 (2014).
- 460 [4] Stranks, S. D. & Snaith, H. J. Metal-halide perovskites for photovoltaic and light-emitting
461 devices. *Nat. Nanotechnol.* **10**, 391–402 (2015).
- 462 [5] Jeon, N. J. *et al.* Compositional engineering of perovskite materials for high-performance solar
463 cells. *Nature* **517**, 476–480 (2015).
- 464 [6] McMeekin, D. P. *et al.* A mixed-cation lead mixed-halide perovskite absorber for tandem solar
465 cells. *Science* **351**, 151–155 (2016).
- 466 [7] Lin, K. *et al.* Perovskite light-emitting diodes with external quantum efficiency exceeding 20
467 per cent. *Nature* **562**, 245–248 (2018).
- 468 [8] Jung, E. H. *et al.* Efficient, stable and scalable perovskite solar cells using poly(3-
469 hexylthiophene). *Nature* **567**, 511–515 (2019).
- 470 [9] Yi, C. *et al.* Entropic stabilization of mixed A-cation ABX₃ metal halide perovskites for high
471 performance perovskite solar cells. *Energy Environ. Sci.* **9**, 656–662 (2016).
- 472 [10] Saliba, M. *et al.* Cesium-containing triple cation perovskite solar cells: Improved stability,
473 reproducibility and high efficiency. *Energy Environ. Sci.* **9**, 1989–1997 (2016).
- 474 [11] Li, N. *et al.* Cation and anion immobilization through chemical bonding enhancement with
475 fluorides for stable halide perovskite solar cells. *Nat. Energy* **4**, 408–415 (2019).
- 476 [12] Zuo, F. *et al.* Binary-Metal Perovskites Toward High-Performance Planar-Heterojunction
477 Hybrid Solar Cells. *Adv. Mater.* **26**, 6454–6460 (2014).
- 478 [13] Hao, F., Stoumpos, C. C., Chang, R. P. & Kanatzidis, M. G. Anomalous band gap behavior
479 in mixed Sn and Pb perovskites enables broadening of absorption spectrum in solar cells. *J.*
480 *Am. Chem. Soc.* **136**, 8094–8099 (2014).
- 481 [14] Anaya, M. *et al.* Optical analysis of CH₃NH₃Sn_xPb_{1-x}I₃ absorbers: A roadmap for perovskite-
482 on-perovskite tandem solar cells. *J. Mater. Chem. A* **4**, 11214–11221 (2016).

- 483 [15] Goyal, A. *et al.* Origin of Pronounced Nonlinear Band Gap Behavior in Lead-Tin Hybrid
484 Perovskite Alloys. *Chem. Mater.* **30**, 3920–3928 (2018).
- 485 [16] Jung, Y. K., Lee, J. H., Walsh, A. & Soon, A. Influence of Rb/Cs Cation-Exchange on
486 Inorganic Sn Halide Perovskites: From Chemical Structure to Physical Properties. *Chem.*
487 *Mater.* **29**, 3181–3188 (2017).
- 488 [17] Beal, R. E. *et al.* Cesium Lead Halide Perovskites with Improved Stability for Tandem Solar
489 Cells. *J. Phys. Chem. Lett.* **7**, 746–751 (2016).
- 490 [18] Noh, J. H., Im, S. H., Heo, J. H., Mandal, T. N. & Seok, S. I. Chemical management for
491 colorful, efficient, and stable inorganic-organic hybrid nanostructured solar cells. *Nano Lett.*
492 **13**, 1764–1769 (2013).
- 493 [19] Eperon, G. E. *et al.* Formamidinium lead trihalide: A broadly tunable perovskite for efficient
494 planar heterojunction solar cells. *Energy Environ. Sci.* **7**, 982–988 (2014).
- 495 [20] Bush, K. A. *et al.* 23.6%-Efficient Monolithic Perovskite/Silicon Tandem Solar Cells With
496 Improved Stability. *Nat. Energy* **2**, 1–7 (2017).
- 497 [21] Rajagopal, A. *et al.* Highly Efficient Perovskite–Perovskite Tandem Solar Cells Reaching 80%
498 of the Theoretical Limit in Photovoltage. *Adv. Mater.* **29**, 1–10 (2017).
- 499 [22] Hoke, E. T. *et al.* Reversible photo-induced trap formation in mixed-halide hybrid perovskites
500 for photovoltaics. *Chem. Sci.* **6**, 613–617 (2015).
- 501 [23] Draguta, S. *et al.* Rationalizing the light-induced phase separation of mixed halide organic-
502 inorganic perovskites. *Nat. Commun.* **8** (2017).
- 503 [24] Wang, X. *et al.* Suppressed phase separation of mixed-halide perovskites confined in endotaxial
504 matrices. *Nat. Commun.* **10**, 1–7 (2019).
- 505 [25] Elmelund, T., Seger, B., Kuno, M. & Kamat, P. V. How Interplay between Photo and Thermal
506 Activation Dictates Halide Ion Segregation in Mixed Halide Perovskites. *ACS Energy Lett.* **5**,
507 56–63 (2020).
- 508 [26] Hu, M., Bi, C., Yuan, Y., Bai, Y. & Huang, J. Stabilized wide bandgap MAPbBr_xI_{3-x}
509 perovskite by enhanced grain size and improved crystallinity. *Adv. Sci.* **3**, 6–11 (2015).
- 510 [27] Yang, Z. *et al.* Stabilized Wide Bandgap Perovskite Solar Cells by Tin Substitution. *Nano*
511 *Lett.* **16**, 7739–7747 (2016).
- 512 [28] Hutter, E. M. *et al.* Thermodynamic stabilization of mixed-halide perovskites against phase
513 segregation. *Cell Reports Phys. Sci.* **1**, 100120 (2020).

- 514 [29] Xu, J. *et al.* Triple-halide wide-band gap perovskites with suppressed phase segregation for
515 efficient tandems. *Science* **367**, 1097–1104 (2020).
- 516 [30] Braly, I. L. *et al.* Current-Induced Phase Segregation in Mixed Halide Hybrid Perovskites
517 and its Impact on Two-Terminal Tandem Solar Cell Design. *ACS Energy Lett.* **2**, 1841–1847
518 (2017).
- 519 [31] Rehman, W. *et al.* Photovoltaic mixed-cation lead mixed-halide perovskites: Links between
520 crystallinity, photo-stability and electronic properties. *Energy Environ. Sci.* **10**, 361–369
521 (2017).
- 522 [32] Dang, H. X. *et al.* Multi-cation Synergy Suppresses Phase Segregation in Mixed-Halide Per-
523 ovskites. *Joule* **3**, 1746–1764 (2019).
- 524 [33] Bischak, C. G. *et al.* Tunable polaron distortions control the extent of halide demixing in lead
525 halide perovskites. *J. Phys. Chem. Lett.* **9**, 3998–4005 (2018).
- 526 [34] Bush, K. A. *et al.* Compositional engineering for efficient wide band gap perovskites with
527 improved stability to photoinduced phase segregation. *ACS Energy Lett.* **3**, 428–435 (2018).
- 528 [35] Tao, S. *et al.* Absolute energy level positions in tin- and lead-based halide perovskites. *Nat.*
529 *Commun.* **10**, 1–10 (2019).
- 530 [36] Bischak, C. G. *et al.* Origin of reversible photoinduced phase separation in hybrid perovskites.
531 *Nano lett.* **17**, 1028–1033 (2017).
- 532 [37] Mao, W. *et al.* Light-induced reversal of ion segregation in mixed-halide perovskites. *Nat.*
533 *Mater.* (2020).
- 534 [38] Knight, A. J. *et al.* Electronic traps and phase segregation in lead mixed-halide perovskite.
535 *ACS Energy Lett.* **4**, 75–84 (2018).
- 536 [39] Belisle, R. A. *et al.* Impact of surfaces on photoinduced halide segregation in mixed-halide
537 perovskites. *ACS Energy Lett.* **3**, 2694–2700 (2018).
- 538 [40] Barker, A. J. *et al.* Defect-assisted photoinduced halide segregation in mixed-halide perovskite
539 thin films. *ACS Energy Lett.* **2**, 1416–1424 (2017).
- 540 [41] Sher, A. *et al.* Quasichemical approximation in binary alloys. *Phys. Rev. B* **36**, 4279–4295
541 (1987).
- 542 [42] Brivio, F., Caetano, C. & Walsh, A. Thermodynamic Origin of Photoinstability in the
543 $\text{CH}_3\text{NH}_3\text{Pb}(\text{I}_{1-x}\text{Br}_x)_3$ Hybrid Halide Perovskite Alloy. *J. Phys. Chem. Lett.* **7**, 1083–1087
544 (2016).

- 545 [43] Johnston, M. B. & Herz, L. M. Hybrid Perovskites for Photovoltaics: Charge-Carrier Recom-
546 bination, Diffusion, and Radiative Efficiencies. *Acc. Chem. Res.* **49**, 146–154 (2016).
- 547 [44] Blöchl, P. E. Projector augmented-wave method. *Phys. Rev. B* **50**, 17953–17979 (1994).
- 548 [45] Perdew, J. P. *et al.* Restoring the density-gradient expansion for exchange in solids and
549 surfaces. *Phys. Rev. Lett.* **100**, 1–4 (2008).
- 550 [46] Perdew, J. P., Burke, K. & Ernzerhof, M. Generalized gradient approximation made simple.
551 *Phys. Rev. Lett.* **77**, 3865–3868 (1996).
- 552 [47] Kresse, G. & Furthmüller, J. Efficient iterative schemes for ab initio total-energy calculations
553 using a plane-wave basis set. *Phys. Rev. B - Condens. Matter Mater. Phys.* **54**, 11169–11186
554 (1996).
- 555 [48] Schleife, A. *et al.* Ab initio description of heterostructural alloys: Thermodynamic and struc-
556 tural properties of $Mg_xZn_{1-x}O$ and $Cd_xZn_{1-x}O$. *Phys. Rev. B - Condens. Matter Mater.*
557 *Phys.* **81**, 1–15 (2010).
- 558 [49] De Carvalho, L. C., Schleife, A., Furthmüller, J. & Bechstedt, F. Distribution of cations in
559 wurtzitic $In_xGa_{1-x}N$ and $In_xAl_{1-x}N$ alloys: Consequences for energetics and quasiparticle
560 electronic structures. *Phys. Rev. B - Condens. Matter Mater. Phys.* **85**, 1–14 (2012).

561 **ACKNOWLEDGEMENTS**

562 The authors thank Prof.dr. René Janssen and MSc Kunal Datta for stimulating discus-
563 sions about the subject of this work. ZC acknowledges funding from Eindhoven University of
564 Technology. ST acknowledges funding by the Computational Sciences for Energy Research
565 (CSER) tenure track program of Shell and NWO (Project No. 15CST04-2) as well as NWO
566 START-UP from the Netherlands.

567 **AUTHOR CONTRIBUTIONS**

568 The project was conceived and planned by PAB and ST. All calculations were done by
569 ZC. ST and GB guided the work on the DFT calculations and PAB guided the work on
570 the phase diagrams. The first version of the manuscript was written by ZC under guidance
571 of PAB. All authors contributed to the results of this work and to the final version of the
572 manuscript.

573 **ADDITIONAL INFORMATION**

574 **Supplementary Information**

575 Supplementary Information accompanies this paper at xxx.

576 **Competing interests**

577 The authors declare no competing financial interests.

Figures

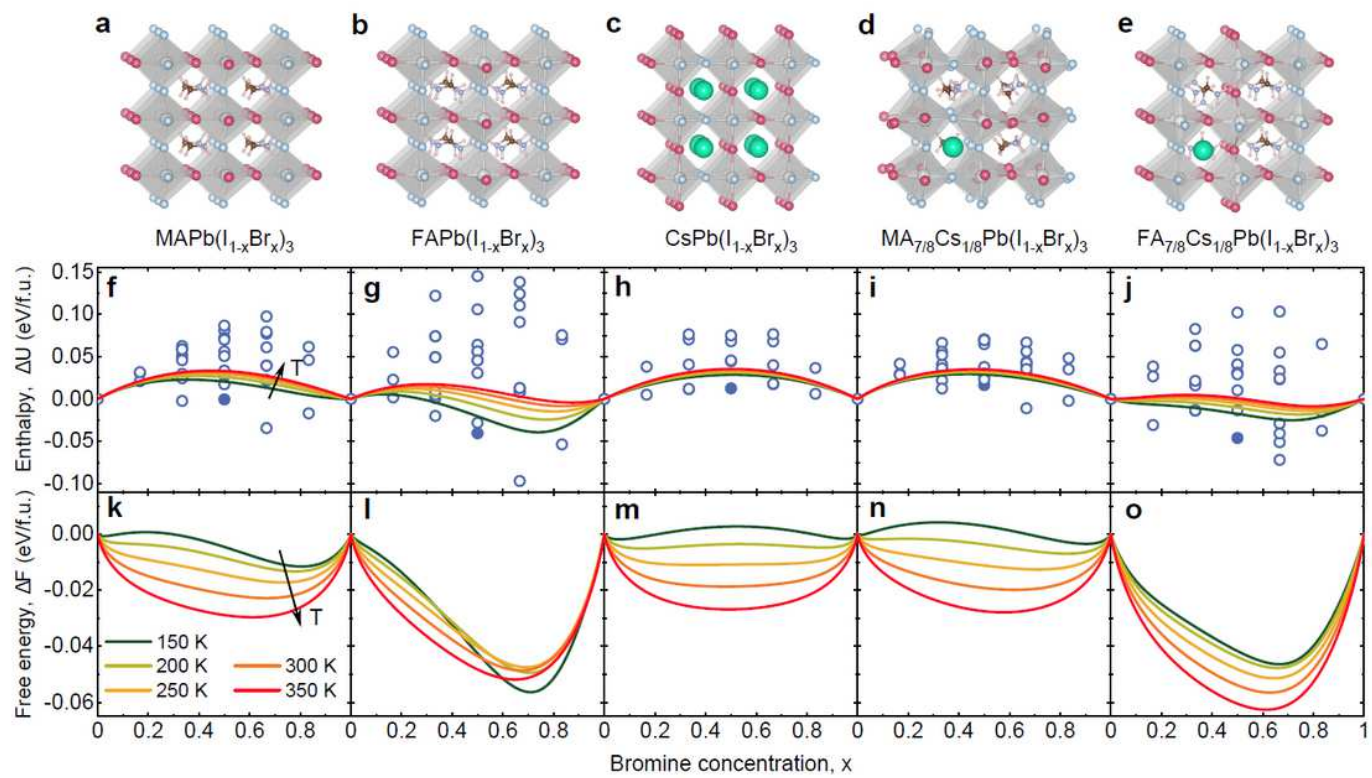
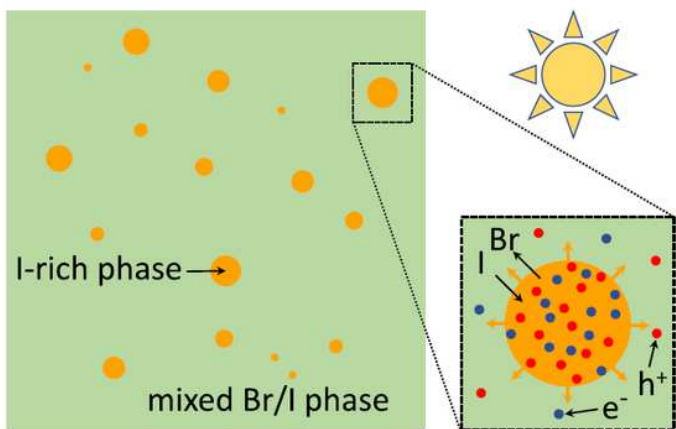
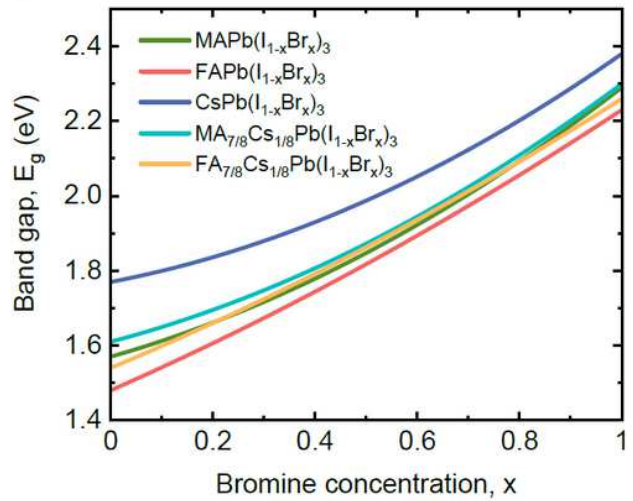


Figure 1

Mixing enthalpy and free energy of mixed I/Br perovskites in the dark. (a)-(e) Atomic structures of the most stable configurations of the different compounds at relative Br concentration $x = 0.5$. Red spheres: I. Blue spheres: Br. White spheres inside octahedra: Pb. Green spheres: Cs. Cationic molecules in between octahedra: methylammonium (MA) or formamidinium (FA). (f)-(j) Mixing enthalpy per formula unit (f.u.) as a function of Br concentration. Circles: values calculated for each mixed configuration. Filled circles: values for the most stable configurations at $x = 0.5$, displayed in (a)-(e). Curves: results for the quasi-chemical approximation (QCA) at different temperatures. (k)-(o) Mixing free energy per formula unit as a function of Br concentration.

a**b****Figure 2**

Mechanism of light-induced halide segregation. (a) Nucleation of an I-rich phase from a mixed I/Br phase under illumination. The compositional free energy favours mixing, but this is dominated by a free energy decrease favouring demixing due to funneling of electrons and holes into low-band gap I-rich nuclei that grow by inward diffusion of I and outward diffusion of Br. (b) Band gap as a function of relative Br concentration x for the different compounds.

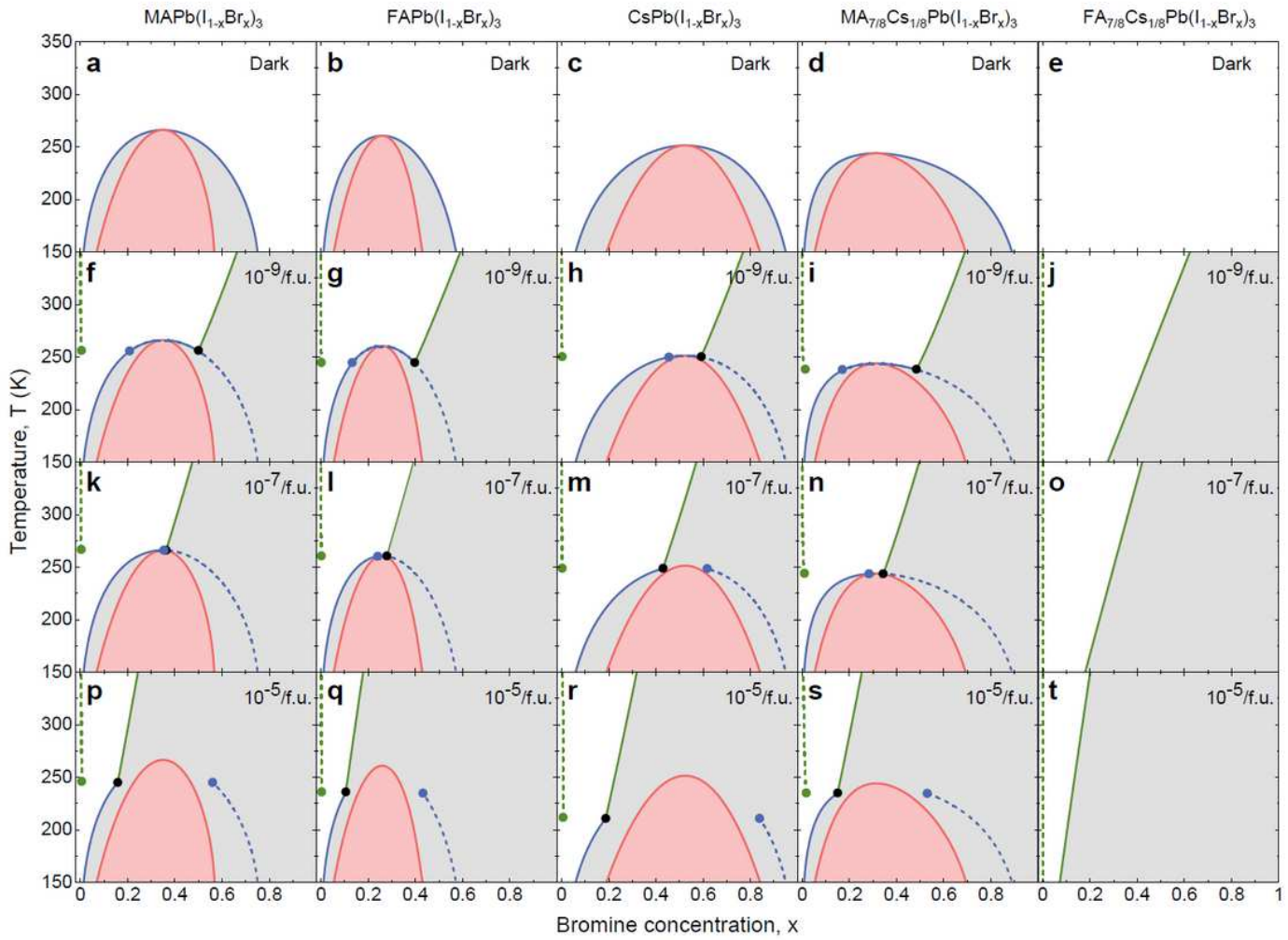


Figure 3

Phase diagrams at different photocarrier densities. (a)-(e) Phase diagrams in the dark of the different compounds in the temperature window 150-350 K. (f)-(t) Phase diagrams for photocarrier densities $n = 10^{-9}, 10^{-7}$, and 10^{-5} per formula unit. Red lines: spinodals separating the metastable (grey) and unstable (pink) regions. Full blue and green lines: binodals separating the stable (white) and metastable regions, with the blue (green) lines indicating the compositional (light-induced) binodals. When entering the metastable region by crossing the compositional (light-induced) binodals, nucleation of a phase with a Br concentration indicated by the dashed blue (green) lines becomes favourable. The dots indicate the possible coexistence of three phases: the parent phase (black dots) and two types of nucleated phases with different Br concentration (blue and green dots).

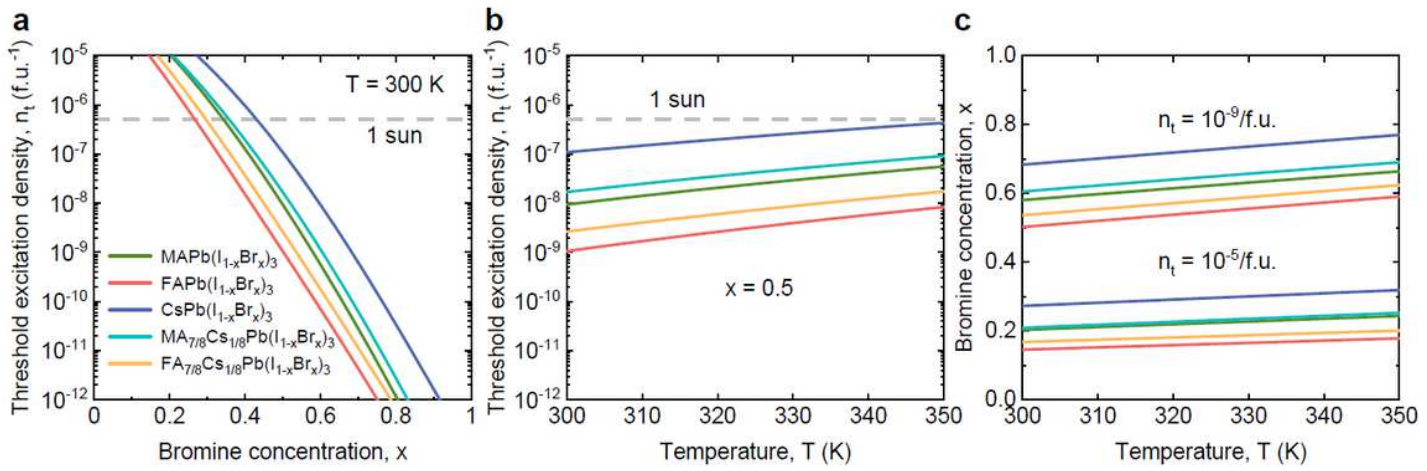


Figure 4

Threshold photocarrier density for light-induced halide segregation. (a) Threshold photocarrier density n_t for the different compounds at room temperature $T = 300$ K for light-induced halide segregation, as a function of Br concentration x . (b) Threshold photocarrier density as a function of temperature for $x = 0.5$. The horizontal dashed line in (a) and (b) indicates the photocarrier density $n = 5 \times 10^{-7}$ /f.u. in the mixed phase for about 1 sun illumination. (c) Bromine concentration as a function of temperature at threshold photocarrier densities $n_t = 10^{-9}$ and 10^{-5} /f.u.

Supplementary Files

This is a list of supplementary files associated with this preprint. Click to download.

- [Supplementary.pdf](#)